Available online at www.sciencedirect.com
SCIENCE DIRECT
NDT&E International 38 (2005) 701–711
NDT&E international
www.elsevier.com/locate/ndteint

Post-processing of the full matrix of ultrasonic transmit–receive array data for non-destructive evaluation

Caroline Holmes, Bruce W. Drinkwater*, Paul D. Wilcox

Department of Mechanical Engineering, University of Bristol, Queen's Building, University Walk, Bristol BS8 1TR, UK

Received 24 January 2005; revised 11 April 2005; accepted 21 April 2005
Available online 15 June 2005

Abstract

Processing of ultrasonic array data is traditionally based on having parallel transmission circuits that enable staggered firing of transmitter elements to produce the desired wavefront. This paper describes an alternative approach in which the full matrix of time domain signals from every transmitter–receiver pair is captured and post-processed. Various post-processing approaches are modelled and assessed in terms of their ability to image a point-like reflector. Experimental results are then presented which show good quantitative agreement with the modelled results. An advanced processing algorithm is also implemented which allows the array to be focused at every point in the target region in both transmission and reception. This approach is shown to offer significant performance advantages for NDE.

Keywords: Ultrasonics; Arrays; Post-processing

1. Introduction

The use of ultrasonic phased array systems for non-destructive evaluation (NDE) has increased dramatically in recent years. Such systems have been used for many years in the field of medical diagnostics [1]. The advantage of using arrays in NDE over conventional single element transducers is the ability to perform multiple inspections without the need for reconfiguration and also the potential for improved sensitivity and coverage. Plane beams, steered angled beams and focused beams [2,3] are often used to increase the range and accuracy of inspection. The recent development of two-dimensional arrays has also led to an increase in interest in three-dimensional volumetric imaging of components [4]. Flexible arrays [5] and high temperature arrays [6] are being developed to allow testing of components with complex geometries, and harsh environments especially for within the aerospace and nuclear industries. In addition air coupled arrays are showing significant promise for NDE [7].

The ultrasonic arrays for NDE are traditionally used to emulate a monolithic transducers. The approach is based on having independently controlled parallel transmission circuits that enable staggered firing of transmitter elements so that the physical wavefront injected into a target specimen can be translated, steered or focused. This allows real time images (B-scans) to be generated. However, in many areas of industrial NDE the target is static and it is reasonable to carry out data analysis offline. Advances in computer power and memory mean that it is relatively quick and easy to process large amounts of data on a standard PC. In this paper an offline post-processing technique is described which utilises the complete set of time-domain data (A-scans) from all combinations of transmit and receive elements. This approach is referred to as full matrix capture (FMC). Although the time required to capture these signals appears at first glance to be large, if the array controller has independent parallel reception channels then FMC can be performed in approximately the same time as a swept aperture B-scan measurement. The advantages of this approach are increased sensitivity to small defects and greater inspection coverage.

The aim of this paper is first to define the underlying mathematics and practical implementation of four post-processing algorithms for use with the full matrix of array data. The algorithms considered are: plane B-scan, focused

* Corresponding author. Tel.: +44 117 928 9749; fax: +44 117 929 4423.
E-mail address: b.drinkwater@bristol.ac.uk (B.W. Drinkwater).

0963-8695/$ - see front matter © 2005 Elsevier Ltd. All rights reserved.
doi:10.1016/j.ndteint.2005.04.002

B-scan, sector B-scan and the total focusing method (TFM) [8]. Note that the plane B-scan, focused B-scan, sector B-scan algorithms emulate standard ultrasonic inspection methodologies. They can be implemented in either a conventional phased array system or by post-processing subsets of information in the full matrix of array data. However, the TFM utilises all the information in the full matrix of array data and can only be practically implemented by post-processing. Secondly, side-by-side quantitative comparisons of these algorithms will be performed. The third aim is to demonstrate that the Total Focusing Method out performs all other algorithms and that it can be implemented experimentally in an NDE context.

2. Simulation of ultrasonic array data

This section describes the model, which has been used to simulate the ultrasonic array data. In this paper this means the full matrix of time domain signals for all transmit and receive combinations. In order to compare the post-processing techniques for use in NDE their ability to image a single point reflector (often termed the point spread function) is assessed. Simulated data is ideal for this task as problems associated with experimental data, such as noise and coupling variation are removed. The generation of the full matrix of array data is described in this section and the implementation of the post-processing algorithms in Section 3.

The array geometry used for the modelling is that of a linear array transducer with equi-spaced elements and is shown in Fig. 1. The elements are assumed to be long in the y-direction and so the model is reduced to two-dimensions, with propagation of energy in the x–z (focal) plane only. The performance of an ultrasonic phased array system can be characterised by its ability to image to a point reflector. The size and shape of the image of the point can be measured laterally (x-direction) and axially (z-direction) as the distance between the −6 dB points on the image.

A two-dimensional simulation program (written using Matlab version 6.5) was used to generate the individual time domain traces for all combinations of transmit (tx) and receive (rx) elements. As an example the operation of

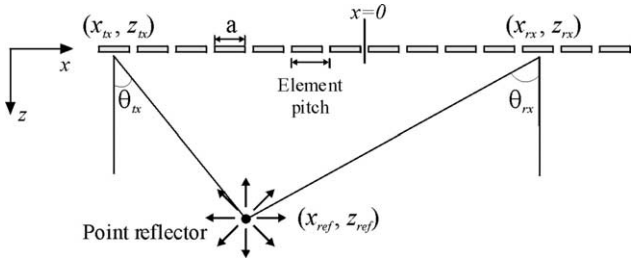

Fig. 1. Phased array geometry.

Table 1
Simulated and experimental array parameters

Array parameter	Value
Number of elements	64
Element width	0.53 mm
Element pitch	0.63 mm
Centre frequency	5 MHz
Bandwidth (−6 dB)	50%

a typical commercial 5 MHz array with 64 elements was modelled. The array had an element pitch of 0.63 mm and element width of 0.53 mm (full details shown in Table 1). At the centre frequency of the transducer the wavelength (in aluminium) was 1.26 mm. As this is twice the element pitch, grating lobes will not be present in the images [9]. The output of each element was a five cycle, Gaussian windowed tone burst with a centre frequency of 5 MHz and a −6 dB bandwidth of 50%. Throughout the modelling a sampling frequency of 100 MHz was used.

The position of a single point reflector within the aluminium was then defined in terms of the x and z coordinates. The propagation distance, $d_{\mathrm{tx,rx}}$ from the transmitter to the reflector and back to the receiver was then calculated for each possible tx–rx combination as follows

$$d_{\mathrm{tx,rx}} = \sqrt{(x_{\mathrm{ref}} - x_{\mathrm{tx}})^2 + (z_{\mathrm{ref}})^2} + \sqrt{(x_{\mathrm{ref}} - x_{\mathrm{rx}})^2 + (z_{\mathrm{ref}})^2} \quad (1)$$

where x_{ref}, z_{ref} are the coordinates of the reflector and the tx and rx subscripts refer to the transmit and receive elements, respectively. Phase shifts were then applied to the element output signal, $f(t)$, to simulate propagation. The propagation time, t, was determined by dividing the propagation distance, $d_{\mathrm{tx,rx}}$ by the longitudinal velocity of sound in aluminium, c_1 (6300 ms^{-1}). The frequency spectrum, $F(\omega)$, can then be calculated from the element output signal using the Fourier transform as follows:

$$F(\omega) = \int_{-\infty}^{\infty} f(t) \mathrm{e}^{i\omega t} \mathrm{d}\omega \quad (2)$$

The complex spectrum of the phase shifted signal $G_{\mathrm{tx,rx}}(\omega)$ is therefore given by:

$$G_{\mathrm{tx,rx}}(\omega) = F(\omega) \mathrm{e}^{(-i\omega/c_1)d_{\mathrm{tx,rx}}} \quad (3)$$

This propagated spectrum is then multiplied by an amplitude factor in order to include the effects of element directivity and beam spread. Following the approach of McNab and Stumpf [10], the directivity $p(\theta, \phi)$ function of a single rectangular element was defined as

$$\mathrm{p}(\theta, \phi) = \mathrm{sin\,c}\left(\frac{\pi a \sin\theta \cos\phi}{\lambda}\right) \mathrm{sin}\, c\left(\frac{\pi \mathrm{L} \sin\theta \sin\phi}{\lambda}\right) \quad (4)$$

where a is the element width, L is the element length and λ is the wavelength of the ultrasonic wave. θ and ϕ are the angles from the element normal in the steering and elevation planes, respectively. In the two-dimensional model used here it is implicitly assumed that $L \gg a$, which is typical of industrial NDE arrays. Therefore, the directivity functions for the transmitting and receiving elements in this case is reduce to the following expressions:

$$p_{\mathrm{tx}} = \sin \mathrm{c}\left(\frac{\pi a \sin\theta_{\mathrm{tx}}}{\lambda}\right) \text{ and } p_{\mathrm{rx}} = \sin c\left(\frac{\pi a \sin\theta_{\mathrm{rx}}}{\lambda}\right) \quad (5)$$

Finally, a two-dimensional inverse power law was used to model the effect of the divergence of the waves from the transmitter and from the point reflector. The amplitude $A_{\mathrm{tx,rx}}$, of the signal after propagating a transmission distance d_{tx} and reflected distance d_{rx} in the medium was calculated using

$$A_{\mathrm{tx,rx}} = \frac{A_0}{\sqrt{d_{\mathrm{tx}} d_{\mathrm{rx}}}} \quad (6)$$

where A_0 is the signal amplitude at unity propagation distance. The resulting spectrum for each transmitter–receiver pair, $H_{\mathrm{tx,rx}}(\omega)$, is the product of the phase shifted element output signal, the directivity function for the transmit and receive elements and the amplitude fraction due to beam spread.

$$H_{\mathrm{tx,rx}}(\omega) = p_{\mathrm{tx}} p_{\mathrm{rx}} A_{\mathrm{tx,rx}} G_{\mathrm{tx,rx}}(\omega) \quad (7)$$

An inverse Fourier transform can then applied to transform the signal back to the time domain, but in practice it is more useful for subsequent post-processing to obtain the complex Hilbert transform [11] of the resulting time domain signal, $h_{\mathrm{tx,rx}}(t)$, given by:

$$h_{\mathrm{tx,rx}}(t) = \frac{1}{\pi}\int_0^{\infty} H_{\mathrm{tx,rx}}(\omega) \mathrm{e}^{-i\omega t} \mathrm{d}\omega \quad (8)$$

This process was carried out for each possible transmitter–receiver pair and allowed a maximum of n^2 possible time domain signals to be generated. However, if it is assumed that the performance of each element is equal throughout the array, there is some redundancy in the data. For example, the signal that is transmitted from element X and received on element Y is identical to the signal transmitted on element Y and received on element X. This redundancy means that only $n/2(n+1)$ signals are required for post-processing.

3. Implementation of post-processing algorithms

In this section three standard inspection techniques currently used in phased array NDE are implemented as post-processing algorithms: plane B-scan, focused B-scan and sector B-scan. An advanced imaging algorithm termed the total focusing method (TFM) is also described and quantitatively compared with the traditional techniques.

3.1. Plane B-scan

If used alone, a single array element would have poor lateral resolution due to the beam divergence and low sensitivity due to the small element size. In order to overcome this a number of adjacent elements, termed an aperture, are pulsed simultaneously as shown in Fig. 2(a) to

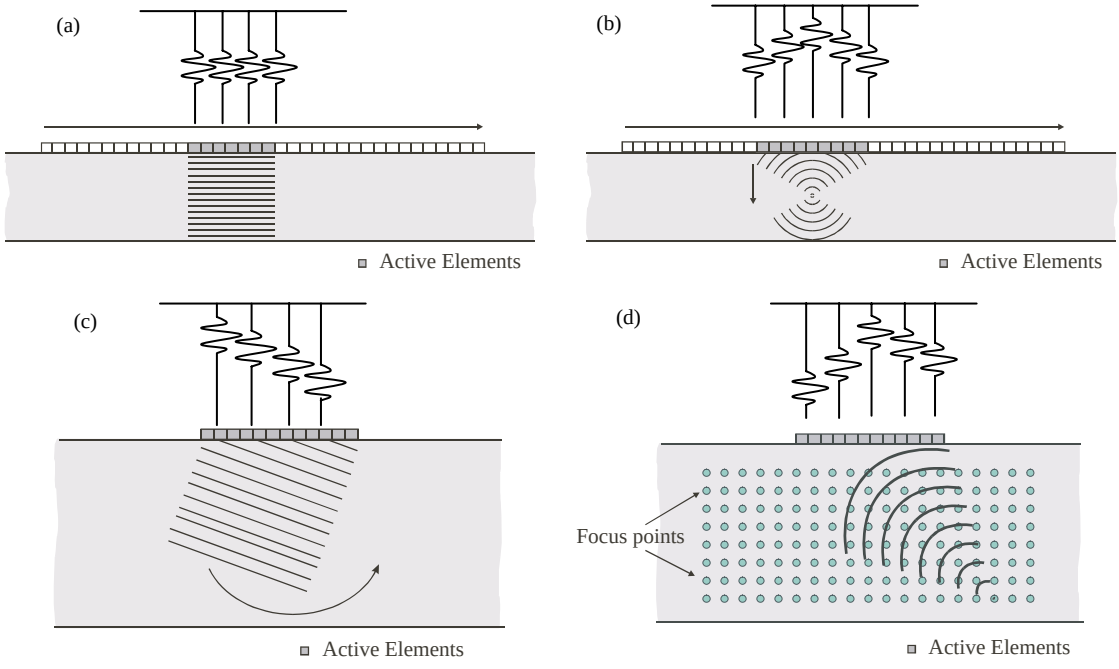

Fig. 2. Schematic diagram of the (a) plane, swept B-scan, (b) focused swept B-scan, (c) sector B-scan and (d) fully focused TFM.

produce a planar beam. The received time domain signals from all the elements in the aperture are then summed to produce a single time domain signal. This approach has the same performance as a plane transducer of the same size as the aperture. The aperture is then electronically shifted along the length of the array, with the time domain signals obtained from each step being combined to form the final B-scan image.

In post-processing, the starting point is the full matrix of array data. The B-scan imaging algorithm sums the parts of the matrix corresponding to the time domain signals from the individual elements in each aperture. Results for different aperture positions are computed from different parts of the matrix. The intensity of a point in the plane B-scan image, $I(x,z)$ is given by

$$I(x,z) = \left| \sum h_{\mathrm{tx,rx}}\left(\frac{2z}{c_1}\right) \right| \quad \text{summed for } |x_{\mathrm{tx,rx}} - x| \le \frac{D}{2} \tag{9}$$

where D is the width of the aperture and z is the distance in the z-direction (i.e. normal to the array surface).

3.2. Focused B-scan

Focusing, either spherical or cylindrical with monolithic ultrasonic transducers, is realised by means of a curved piezoelectric element or lens. In conventional phased array systems, the elements within an aperture can be used to produce a focused beam by introducing time delays at both the transmission and reception stages as shown in Fig. 2(b). These delays mean that the emitted pulses arrive in phase at one particular region, which produces a high intensity focal zone. The reflected signals are then delayed in reception (typically by the same amount as on transmission) and summed. This is similar to the synthetic aperture focusing technique (SAFT) which typically uses a single transducer and so only the pulse echo signals can be collected [12–14].

Some advanced NDE array systems are capable of focusing at a number of depths below the aperture before stepping to the next set of elements. In transmission this is achieved by multiple firings with different delay sequences. Because increasing the number of firings reduces the overall frame rate, this number of different focal depths on transmission is limited. Currently on reception, the number of delay sequences, which can be implemented is only limited by computational power. Hence commercial dynamic depth focusing systems favour a small number of broad focal zones in transmission with finer focal control on reception [15].

In post-processing of the FMC data the number of focal depths in transmission and reception is unlimited and any array aperture can be focused. Hence the intensity of a point in the image, $I(x, z)$, is given by

$$I(x,z) = \left| \sum h_{\mathrm{tx,rx}}\left(\frac{\sqrt{(x_{\mathrm{tx}}-x)^2+z^2}+\sqrt{(x_{\mathrm{rx}}-x)^2+z^2}}{c_1}\right) \right| \quad \text{summed for } |x_{\mathrm{tx,rx}} - x| \le \frac{D}{2} s \tag{10}$$

where D is the width of the aperture and all other symbols have their usual meanings. Note that linear interpolation of $h(t)$ is required as this function only exists at discrete points in time. The aperture is then stepped along the array, which forces the lateral resolution in the final B-scan, Δx to be fixed and equal to the element pitch. The amplitude at each point in front of the aperture is then calculated by summing the contributions from each tx–rx pair.

3.3. Sector B-scan

A sector B-scan is somewhat different to a plane and focused B-scan since it uses all elements to steer the beam through an angular sweep as shown in Fig. 2(c). Each incremental steering angle generates one scan line in the final image. A traditional steered-beam, phased-array system requires a unique element pulse sequence for each scan line since each line has its own unique steering angle with respect to the transducer face. This type of beam steering requires sophisticated, high-speed pulsing of each individual element. In order to generate each line in the image in post-processing, signals are summed with appropriate time delays to represent the aperture facing in the required direction. The intensity of final B-scan image $I(r,\theta)$ is then generated in polar co-ordinates by linear interpolation of the time domain signals as in the focused B-scan

$$I(r,\theta) = \left| \sum h_{\mathrm{tx,rx}}\left(\frac{2r + x_{\mathrm{tx}}\sin\theta + x_{\mathrm{rx}}\sin\theta}{c_1}\right) \right| \quad \text{summed for all tx, rx} \tag{11}$$

where r is the propagation distance in the beam axis direction measured from the centre of the array and θ is the required beam steer angle with respect to the array normal.

3.4. Total focusing method (TFM)

In the total focusing method (TFM) the beam is focused at every point in the target region as shown in Fig. 2(d). Although this approach has been suggested by a number of authors [8,16] it has yet to be utilised in industrial NDE systems due to a combination of the high number of transmit delay sequences and the computational power required to perform the receive focussing. However, if the full matrix capture approach is adopted then the TFM can be implemented in post-processing, the only limiting factor being computation time.

The TFM post-processing algorithm proceeds by first discretising the target region (in the x, z plane) into a grid.

The signals from all the elements in the array are then summed to synthesise a focus at every point in the grid. The intensity of the image, $I(x, z)$ at any point in the scan is given by:

$$I(x,z) = \left| \sum h_{\mathrm{tx,rx}} \left(\frac{\sqrt{(x_{\mathrm{tx}} - x)^2 + z^2} + \sqrt{(x_{\mathrm{rx}} - x) + z^2}}{c_1} \right) \right| \quad \text{for all tx, rx} \tag{12}$$

As before, linear interpolation of the discretely sampled time domain signals is necessary. This summation is carried out for each possible transmitter–receiver pair and therefore uses the maximum amount of information available for each point.

3.5. Measuring array performance

Fig. 3(a–c) show post-processed focused and sector B-scan images in the x–z plane for simulated data, using the array shown in Table 1. These images show predicted results obtained for a single point reflector located on the centre-line of the array (i.e. $x = 0$) and at a distance of 20λ (25.2 mm) in the z-axis. In each case, a 16 element aperture was used, as this is typical of the aperture sizes used in industrial phased array NDE applications. It can be seen by comparing Fig. 3(a) with Fig. 3(b) that, as expected, the image resolution is increased when focusing is applied. This image enhancement is seen as a reduction in the apparent size of the image of the point reflector. It is worth noting that as the size of the aperture increases the field of view decreases for the plane and focused B-scans. In the extreme, if all 64 elements are used in a plane or focused B-scan, the image is reduced to a single time domain plot, as the aperture can no longer be swept. Fig. 3(d) shows the image obtained using the TFM algorithm. This algorithm is able to fully exploit the focusing capability of the 64 element array and also allows the image to be constructed beyond the edge of the array. In addition, it can be seen that the image resolution is increased when compared to the focused B-scan.

It is useful to quantitatively compare the performance of an array inspection strategy in terms of its ability to detect and image a point-like reflector. In this paper a parameter termed, the array performance indicator (API), has been defined to aid this quantification. Fig. 4 illustrates schematically the concept of API for a simple Gaussian shaped point spread function. The API is a dimensionless measure of the spatial size of a point spread function. It is defined as the area, $A_{-6\ \mathrm{dB}}$, within which the point spread function is greater than -6 dB down from its maximum value, normalised to the square of the wavelength

$$\mathrm{API} = \frac{A_{-6\ \mathrm{dB}}}{\lambda^2} \tag{13}$$

For example, the APIs for each of the scans shown in Fig. 3 are summarised in Table 2. If the plane B-scan is taken as the baseline, it can be seen that the API is reduced by 27% in the focused B-scan using the same number of elements and by 80% in the TFM image.

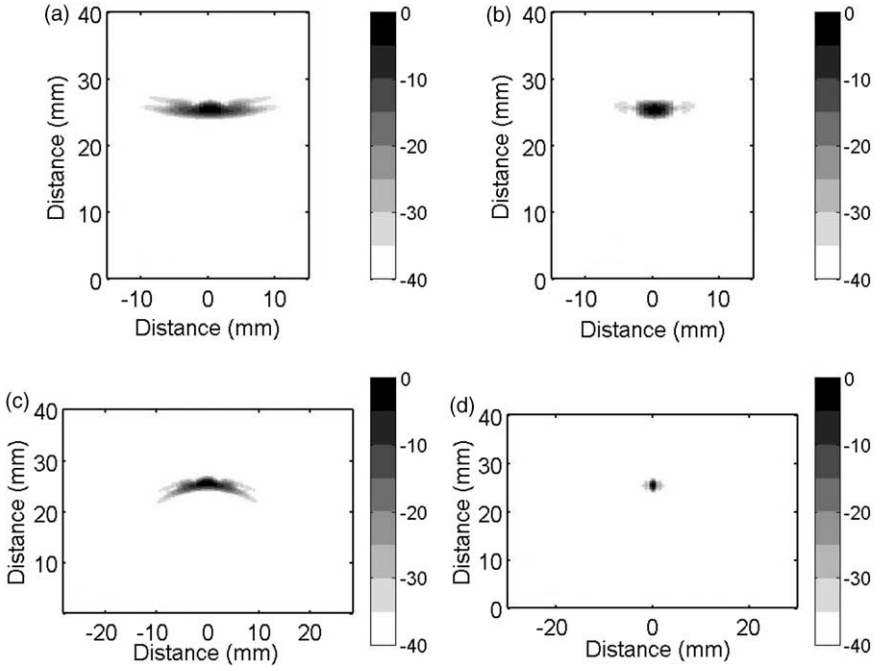

Fig. 3. Simulated images for (a) a plane B-scan, (b) focussed B-scan, (c) sector B-scan and (d) TFM scan. (scale in dB).

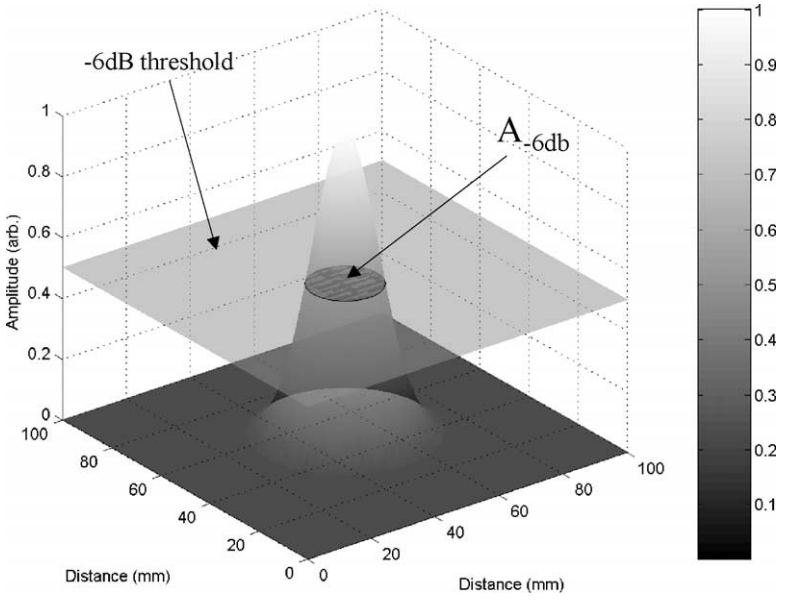

Fig. 4. Schematic representation of the concept of API.

3.6. Modelling results and discussion

Using the array detailed in Table 1 as an example, the processing algorithms described in Sections 3.1–3.4 were assessed by recording the API for a number of reflector positions. The reflector position was varied over a region of 63 mm×63 mm (corresponding to 50λ by 50λ) and an API contour map was produced for point reflectors positioned at regular intervals in the x–z plane. Fig. 6 shows the API contour map obtained for a plane B-scan with 8, 16 and 32 element apertures. The contour lines represent constant API, with the best performance represented by the darker grey scale. It can be seen that as the number of elements in the aperture increases, the effective field of view of the array is reduced and the point of best performance (i.e. just beyond the near field length) appears further away from the array. Fig. 5 also shows regions in which the reflection from the point-like reflector extends beyond the edge of the image. If more than half the image was received its API was calculated assuming symmetry.

Fig. 6 shows the API contour map for an eight element sector B-scan. The API for a sector scan with a 0° steering angle relative to the array normal as indicated by the dotted line on Fig. 6 is identical to that obtained for a plane B-scan with the same aperture (e.g. Fig. 5(a)). Fig. 7 shows the API contour maps obtained for a focused B-scan using 8, 16 and 32 element apertures. It can be seen that, as expected the focused B-scan performs significantly better than either the plane B-scan or sector scan. However, by comparing Figs. 5(a)–7(a) along the central axis and beyond the near field distance of the aperture the performance of the algorithms is similar. It can also be seen from Fig. 8 that there is a trade-off between the viewable area and the maximum performance due to focusing. In Fig. 8 the 32 element focused B-scan (Fig. 8(a)) is compared with the TFM image (Fig. 8(b)) for the same array. The TFM imaging algorithm uses all 64 elements to focus and the performance is therefore improved due to the increased aperture size. In addition, there is a much larger imaging area, which can be covered when using the TFM. It is worth noting that the contours of constant API for the TFA are approximately circular intersecting with the edges of the array. This shape can be deduced from simple geometry if it is assumed that the API is governed the aperture angle. This is because the locus of the apex of a triangle of constant apex angle (i.e. aperture angle), the sides of which pass though two points located at either end of the array, is a circle.

4. Experimental validation

4.1. Experimental apparatus

An experimental data acquisition system was designed and built as shown in Fig. 9. An experimental array was manufactured (Imasonic, France) with the same dimensions and ultrasonic properties as used to calculate the simulated data (i.e. Table 1). The array was connected to a custom

Table 2
Modelled API for images with point reflector at (0, 20λ)

Image type	API
Plane B-scan	2.35
Focused B-scan	1.71
Sector B-scan	2.33
TFM	0.46

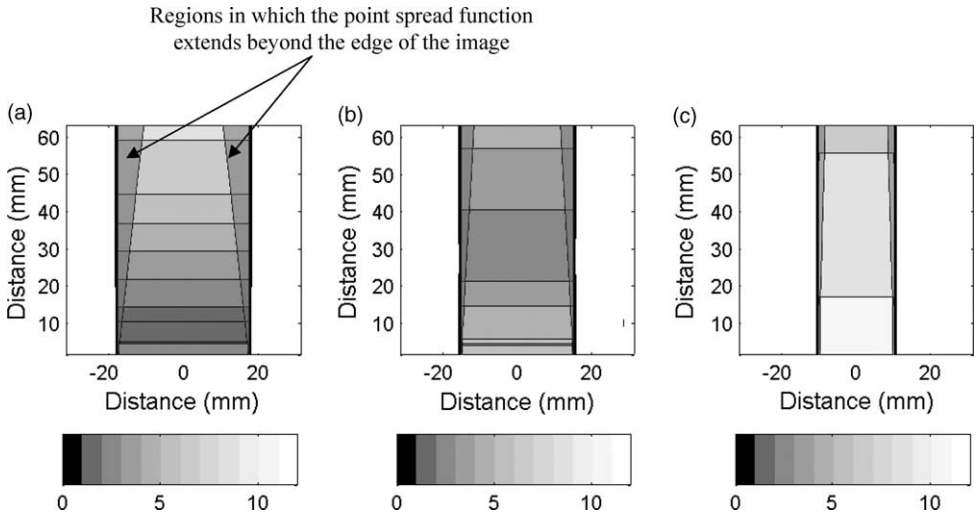

Fig. 5. Simulated plane B-scan API contour maps for (a) 8 elements, (b) 16 elements and (c) 32 elements.

designed signal routing device known as the matrix array controller (MAC). This allowed the transmitted and received signals from a standard single channel pulser-receiver to be independently routed to any pair of elements in the array. The MAC was controlled by a standard PC and was capable of switching between elements at the rate of four per second. A digital storage oscilloscope (DSO) was used to capture the signal received from the array and perform a number of consecutive averages. The averaged signal was then sampled and saved by the controlling PC at a sample rate of 100 MHz and a digital resolution of 16 bits. For each experiment, all pulse-echo and independent pitch-catch signals were captured for offline post-processing. In order to reduce the time taken to complete the data set, redundant signals (i.e. reciprocals of captured transmit–receive combinations) were not captured. This meant that a total of 2080 time domain signals were captured for each experiment.

Three aluminium blocks 200 mm long and 100 mm wide were manufactured with thicknesses of 70, 50, 30 mm. EDM notches 0.3 mm wide and 10 mm in length were cut into one face of each block as shown in Fig. 9. This allowed the array to be placed on the top surface and located above the tip of the EDM notch, thus the tip of the notch emulated the point reflector used in the simulated results. The vertical (z-axis) distances of the reflectors from the array were 60, 40 and 20 mm, which corresponds to approximately 50λ, 30λ and 15λ. The position of the reflector in the x-axis with respect to the array centre ($x=0$) could be easily adjusted by moving the array on the top surface of the block.

4.2. Experimental results and comparison with model

Fig. 10 shows a focused B-scan with 32 elements and a TFM image obtained from post-processing experimental data from the 50 mm aluminium block. In each case, the image was normalised to the maximum amplitude in the back face reflection and is shown in a decibel scale. It can be seen that the tip of the EDM notch and the back face of the block are clearly visible in each case. The API for each algorithm and the signal to incoherent noise ratio (SNR) is shown in Table 3. The SNR was calculated as the ratio of the EDM tip reflection amplitude to the average of the background noise level in the image. The average background noise level was calculated in an area 5 mm by 5 mm in the centre of the image where there was no reflector present.

It can be seen from Table 3 that the API for the focused B-scan and the TFM are significantly lower than for the plane B-scan. It can also be seen that the API for the TFM is approximately half that of the focused B-scan. Fig. 11 shows

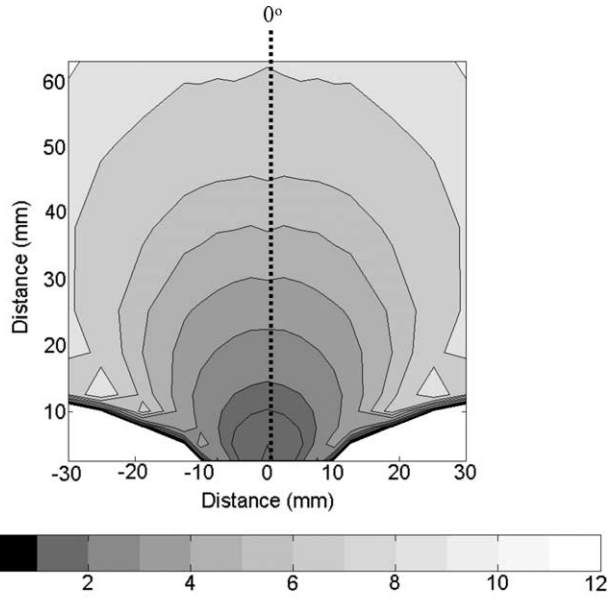

Fig. 6. Simulated sector B-scan API contour map.

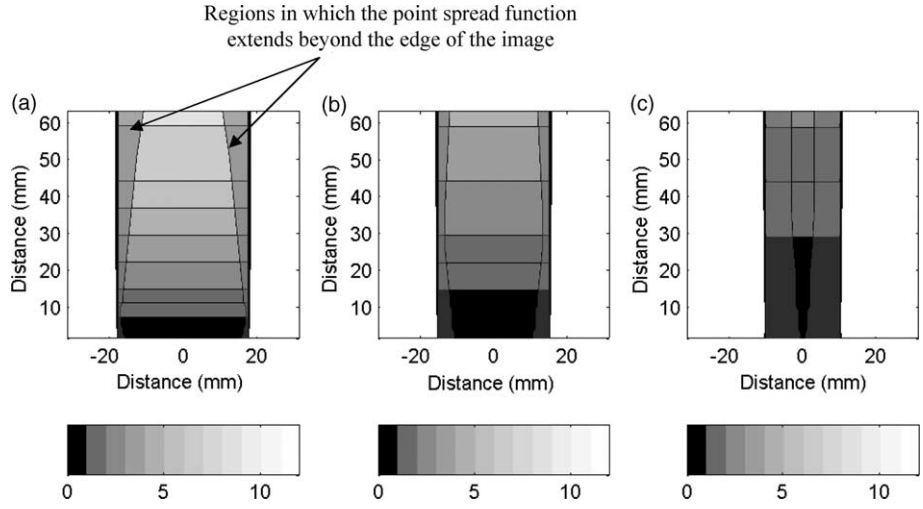

Fig. 7. Simulated focused B-scan API contour maps for (a) 8 elements, (b) 16 elements and (c) 32 elements.

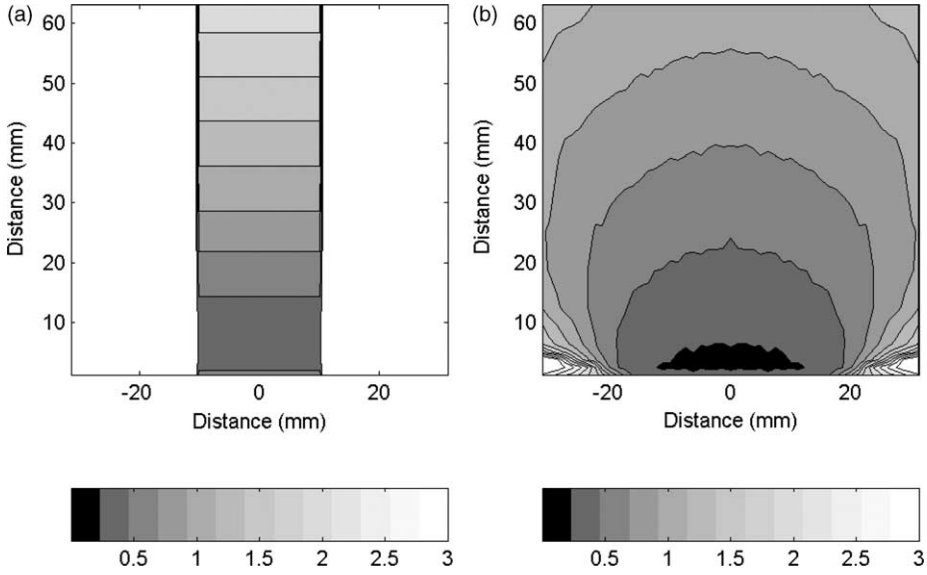

Fig. 8. Simulated API contour map for (a) focused B-scan with 32 elements and (b) TFM using all 64 elements.

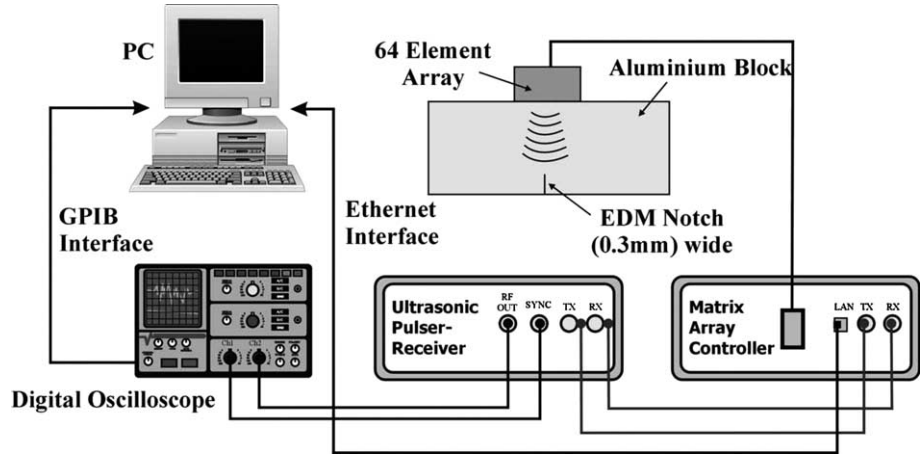

Fig. 9. Schematic diagram of experimental apparatus.

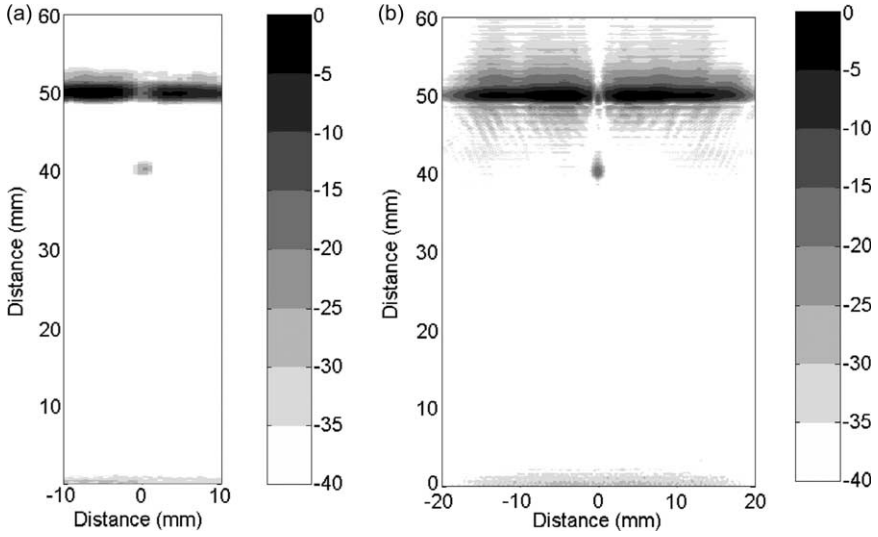

Fig. 10. Experimental images of an EDM notch in a 50 mm thick aluminium block using (a) focused B-scan with 32 elements and (b) TFM with 64 elements.

experimental and simulated TFM images for a reflector positioned at $x=0$, $z=40$ mm in the aluminium block. These images show good consistency between the model and experimental data. The API of the point spread function from the experimental EDM notch tip and the predicted point spread function were calculated as 0.77 and 0.67, respectively. This equates to a difference of 14%, which can be explained by examining the shape of the point spread functions in detail. Fig. 11(c) and (d) show enlarged images of the experimental and predicted point spread functions. It can be seen that in the lateral direction, the width of the point spread function is approximately equal in each case. However, the experimental point spread function is larger in the axial direction. This can be explained by a difference between the bandwidth of the simulated input signal and that produced by the experimental array.

Fig. 12 shows the API for the TFM obtained from a number of experimental results and compared with the corresponding simulated data. It can be seen that the experimentally obtained APIs are consistently higher than the simulated values. This is due to the difference in the bandwidth of the input signals as described above. These results are encouraging as it is the focusing algorithm, which affects the performance in the lateral x-direction whereas, the performance in the axial z-direction is mostly a function of the transducer characteristics.

5. Discussion and conclusions

This paper has described an investigation into the performance of a number of post-processing algorithms for use in NDE. The algorithms were applied to the 'full matrix' of time domain signals from all possible combinations of transmit–receive element pairs. The performance of each algorithm was compared by quantifying its ability to image a point-like reflector (i.e. the point spread function). Experimentally this approach was validated using the reflection from the tip of a 0.3 mm wide EDM notch.

It has been shown that the best performance of the array was achieved using a total focusing method in which the beam is focused at every point in the target region. This method also allows the image to be extended beyond the edge of the array whilst still allowing the beam to focus. This is a significant improvement from swept aperture plane and focused B-scans whose viewable area is dependent on the number of elements used in the aperture. The algorithms were tested using experimental and simulated data and good quantitative agreement was obtained.

In conventional phased array systems, all array elements are fired simultaneously to form a beam with a fixed focus. Using full matrix capture of all transmit–receive combinations allows emulation of any beam-forming scheme through offline post-processing. This approach has some wide ranging design implications for future NDE array systems. However, the main drawback is that using only a single element in transmit limits the total acoustic power output and hence degrades the signal to random noise ratio (SNR) of each transmit–receive pair relative to traditional multi-element aperture approaches. This degradation is tempered by an improvement in SNR due to the averaging effect of the TFM. The net effect is that the SNR of data reconstructed from FMC compared to that obtained from an

Table 3
Results of post-processing experimental data from a 50 mm thick aluminium block

Processing algorithm	API	SNR (dB)
Plane B-scan	15.98	21.5
Focused B-scan	1.52	36.2
TFM	0.77	42.8

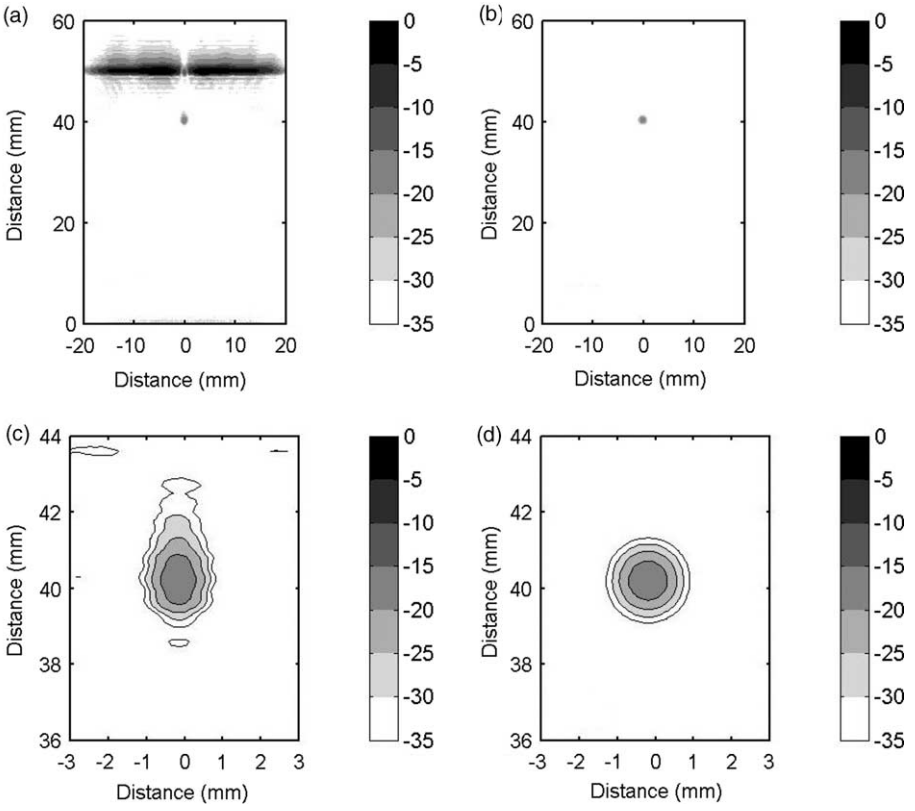

Fig. 11. TFM images of (a) experimental data, (b) model data, (c) experimental data point spread function and (d) model data point spread function.

equivalent multi-channel parallel transmitter is reduced by an amount which is proportional to the square root of the number of elements in the traditional multi-element aperture. For example, in a conventional phased array system, firing 64 elements together to form a beam corresponds to a SNR improvement of 18 dB relative to reconstructing the same beam from FMC data. If the signal to random noise ratio is an issue this can be improved by averaging or use of encoded signals such as Golay sequences [17]. In the current paper, signal averaging over 20 successive acquisitions was performed on the received signal by the DSO. A total of 20 averages corresponds to an increase in the SNR by 13 dB as the SNR is improved in proportion to the square root of the number of averages. This signal averaging was the time limiting factor in the experiments described in this paper. The system described in this paper is currently a laboratory system designed for flexibility rather than speed.

It is instructive to briefly discuss the possible speed that could be realised with a commercial system. In order to perform FMC, the time-trace from each possible pair of transmitter and receiver elements in the array must be captured independently. While this prevents simultaneous transmission, it does not prevent parallel reception and in the optimal system the signals from all elements would be received and captured simultaneously. In this case, the time taken to perform FMC is limited by the time taken to fire each element in the array in turn. The number of separate firings is therefore equal to the number of elements in the array. An element can only be fired after the reverberating echoes due to the firing of the previous element have subsided to an acceptably low level, which defines the maximum pulse-repetition frequency (PRF) that can be achieved. Hence the minimum possible time required to perform FMC is physically limited to the number of elements in the array divided by the maximum PRF. It is worth noting that the minimum time required to perform FMC is not significantly longer than that required to perform a conventional swept B-scan where the active

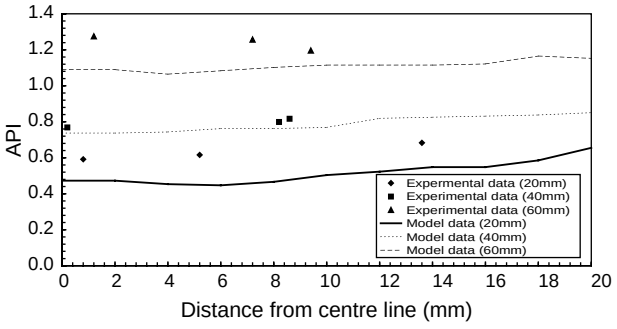

Fig. 12. Comparison between experimental and simulated API obtained from TFM images (figures in brackets indicate axial distance from array to crack tip).

aperture is translated by one element position on each firing cycle. In the swept B-scan the required number of separate firings is equal to the number of aperture positions, which is approximately equal to the number of elements in the array. This discussion has assumed that the time taken to store and process the FMC data is faster than the time taken to acquire it. While this may not be the case at present, it is the opinion of the authors that with the appropriate dedicated hardware and given the rate of advance in computational speed that this will be a valid scenario in the near future.

A further advantage of using full matrix capture is that advanced NDE processing, such as tandem probes, time of flight diffraction and so forth can be carried out on the same data (at a future date) without the need for further experiments. It also ensures that the captured raw data is fully auditable.

Acknowledgements

This work was funded by the EPSRC via the UK Research Centre for Non-Destructive Evaluation (RCNDE).

References

[1] Angelsen BJ, Torp H, Holm S, Kristoffersen J, Whittingham T. Which transducer array is best? Eur J Ultrasound 1995;2:151–64.
[2] Brotherhood CJ, Drinkwater BW, Freemantle RJ. An ultrasonic wheel-array sensor and its application to aerospace structures. Insight 2003;45(11):729–34.
[3] Clay A, Wooh S-C, Azar L, Wang J-Y. Experimental study of phased array beam steering characteristics. J Nondestr Eval 1999;18(2):59–71.
[4] Mendelsohn Y, Wiener-Avnear E. Simulations of circular 2-D phase-array ultrasonic imaging transducers. Ultrasonics 2002;39(9):657–66.
[5] Chatillon S, Cattiaux G, Serre M, Roy O. Ultrasonic non-destructive testing of pieces of complex geometry with flexible phased array transducers. Ultrasonics 2000;38(1–8):131–4.
[6] Kirk KJ, McNab A, Cochran A, Hall I, Hayward G. Ultrasonic arrays for monitoring cracks in an industrial plant at high temperatures. IEEE Trans Ultrason Ferroelectr Freq Control 1999;46(2):311–9.
[7] Neild A, Hutchins DA, Robertson TJ, Davies LAJ, Bilson DR. The radiated fields of focussing air-coupled ultrasonic phased arrays. Ultrasonics 2005;43(3):183–95.
[8] Oralkan O, Sanh Ergun A, Johnson JA, Karaman M, Demirci U, Kaviani K, et al. Capacitive micormachined ultrasonic transducers: next generation array for acoustic imaging? IEEE Trans Ultrason Ferroelectr Freq Control 2002;49(11):1596–610.
[9] Pompei F, Wooh S-C. Phased array element shapes for suppressing grating lobes. J Acoust Soc Am 2002;111(5):2040–8.
[10] McNab A, Stumpf I. Monolithic phased array for the transmission of ultrasound in NDT. Ultrasonics 1986;24(3):148–55.
[11] Kino GS. Acoustic waves: devices, imaging and analogue signal processing. New Jersey: Prentice-Hall; 1987.
[12] Mayer K, Marklein R, Langenberyg KJ, Kreutter T. Three dimensional imaging system based on Fourier transform synthetic aperture focusing technique. Ultrasonics 1990;28(4):241–55.
[13] Ozaki Y, Sumitani T, Tomoda T, Tanaka M. A new system for real-time synthetic aperture ultrasonic imaging. IEEE Trans Ultrason Ferroelectr Freq Control 1988;35(6):828–38.
[14] Chahbaz A, Sicard R. Comparitive evaluation between ultrasonic phased array and synthetic aperture focusing techniques. Review of progress in quantitative nondestructive evaluation. vol. 22. Bellingham, USA: American Institute of Physics; 2002 p. 769–76.
[15] Kremkau F. Diagnostic ultrasound: principles and instruments. Philadelphia, PA: WB Saunders Company; 2002.
[16] Chiao RY, Thomas LJ. Analytical evaluation of sampled aperture ultrasonic imaging techniques for NDE. IEEE Trans Ultrason Ferroelectr Freq Control 1994;41(4):484–93.
[17] Chiao RY, Hao XH. Coded excitation for diagnostic ultrasound: a system developer's perspective. IEEE Trans Ultrason Ferroelectr Freq Control 2005;52(2):160–70.